Received: 31 January 2020 | Revised: 31 August 2020 | Accepted: 6 September 2020
DOI: 10.1002/nbm.4413

RESEARCH ARTICLE

NMR IN BIOMEDICINE WILEY

SNR Weighting for Shear Wave Speed Reconstruction in Tomoelastography

Cemre Ariyurek[1,2] | **Bilal Tasdelen**[1,2] | **Yusuf Ziya Ider**[1] | **Ergin Atalar**[1,2]

[1]Department of Electrical and Electronics Engineering, Bilkent University, Ankara, Turkey

[2]National Magnetic Resonance Research Center (UMRAM), Bilkent University, Ankara, Turkey

Correspondence
Ergin Atalar, Department of Electrical and Electronics Engineering, Bilkent University, Ankara, Turkey.
Email: ergin.atalar@bilkent.edu.tr

Funding information
Türkiye Bilimsel ve Teknolojik Araştirma Kurumu, Grant/Award Number: 117E817

In tomoelastography, to achieve a final wave speed map by combining reconstructions obtained from all spatial directions and excitation frequencies, the use of weights is inevitable. Here, a new weighting scheme, which maximizes the signal-to-noise ratio (SNR) of the final wave speed map, has been proposed. To maximize the SNR of the final wave speed map, the use of squares of estimated SNR values of reconstructed individual maps has been proposed. Therefore, derivations of the SNR of the reconstructed wave speed maps have become necessary. Considering the noise on the complex MRI signal, the SNR of the reconstructed wave speed map was formulated by an analytical approach assuming a high SNR, and the results were verified using Monte Carlo simulations (MCSs). It has been assumed that the noise remains approximately Gaussian when the image SNR is high enough, despite the nonlinear operations in tomoelastography inversion. Hence, the SNR threshold was determined by comparing the SNR computed by MCSs and analytical approximations. The weighting scheme was evaluated for accuracy, spatial resolution and SNR performances on simulated phantoms. MR elastography (MRE) experiments on two different phantoms were conducted. Wave speed maps were generated for simulated 3D human abdomen MRE data and experimental human abdomen MRE data. The simulation results demonstrated that the SNR-weighted inversion improved the SNR performance of the wave speed map by a factor of two compared to the performance of the original (i.e., amplitude-weighted) reconstruction. In the case of a low SNR, no bias occurred in the wave speed map when SNR weighting was used, whereas 10% bias occurred when the original weighting (i.e., amplitude weighting) was used. Thus, while not altering the accuracy or spatial resolution of the wave speed map with the proposed weighting method, the SNR of the wave speed map has been significantly improved.

KEYWORDS
FEM simulations, Monte Carlo simulations, multifrequency magnetic resonance elastography, shear wave speed, SNR

Abbreviations: AWGN, additive white Gaussian noise; DFT, discrete Fourier transform; EP, experimental phantom; EPI-SE, spin-echo echo-planar imaging; FEM, finite element method; MCS, Monte Carlo simulations; MEG, motion encoding gradient; MMRE, multifrequency magnetic resonance elastography; MRE, magnetic resonance elastography; OSS, octahedral shear strain; RMS, root mean square; ROI, region of interest; SD, standard deviation; SNR, signal-to-noise ratio; SP, simulation phantom.

© 2020 John Wiley & Sons, Ltd.

1 | INTRODUCTION

Magnetic resonance elastography (MRE) is a noninvasive technique to measure the mechanical properties of tissues for detecting elasticity alterations due to a pathological state.[1] In MRE, shear waves are induced into the tissue by periodic sinusoidal displacement using a mechanical actuator. Using the shear wave displacement information obtained by the motion encoded phase-difference images, the elastography map is reconstructed. There are a number of reconstruction techniques for generating elastography maps from shear wave displacement data.[2-12]

Tomoelastography,[9] also known as k-MDEV, reconstruction has been shown to be quite successful for the liver, spleen, and mouse brain.[13] Moreover, tomoelastography is a multifrequency MRE technique (MMRE), in which MR elastography data are collected and processed for multiple excitation frequencies to generate the elasticity map. With single frequency excitation, amplitude nulls of the shear wave displacement can be observed in some regions of the tissue being imaged, which may result in an inaccurate estimation of the elasticity of that region.[8,9] Fortunately, using MMRE, the error due to low elastic strain in one frequency at a given location is compensated for by high elastic strain in another frequency. Consequently, the influence of the amplitude nulls on the elastogram is reduced. Here, it should be emphasized that in multifrequency inversion techniques, the frequency dependence of the wave speed (or complex shear modulus)[14,15] is ignored, and its value is averaged in the range of examined excitation frequencies along with direction components.[7,9]

In tomoelastography, the wave speed distribution in the body is computed for each of the directions and frequencies. Then, the computed wave speed distributions are weighted averaged with the fourth power of amplitude of the displacement in each direction and frequency. This amplitude weighting allows only the wave speed distributions that are computed from waves with amplitudes to contribute to the averaging. It should be noted that for single frequency studies, there are similar weighting schemes based essentially on amplitude to combine reconstructions from multiple directions.[5,16]

The type of weighting can and should be designed according to which elastography map feature is desired to be optimized. One idea can be combining multi-inversion results in a way that will yield the elastogram with the maximum possible signal-to-noise ratio (SNR).[17] This aim can be achieved by combining multi-inversion results by weighting with the SNR of the wave speed maps obtained for different directions and frequencies.

To use SNR weighting, SNR distributions of individual wave speed maps for each of the directions and frequencies are required. SNR of the wave-speed maps cannot be estimated directly from the wave-speed maps because of the nonlinear operations in the tomoelastography inversion technique. However, considering the noise on the complex MRI signal, the SNR of the reconstructed elasticity map can be formulated analytically. The findings can be beneficial for combining multidirectional, multifrequency MRE data to obtain high-quality elasticity maps. Unfortunately, there are only a few studies on the SNR in MR elastography (MRE),[18,19] which are designed to understand the quality of the acquired data. Moreover, the SNR of the elasticity map has not yet been investigated. There are acquisition techniques developed for increasing the SNR of the recorded MR data, as proposed in Johnson et al[20] and summarised in Guenthner et al.[21]

In this study, we analyze the SNR of wave speed maps obtained with tomoelastography inversion by analytically deriving the SNR at each step of the algorithm, with the assumption of a high SNR. Then, the minimum SNR value that our analytical derivation holds for is determined by Monte Carlo simulations (MCSs). Later, optimum weights to maximize the SNR of the wave speed map are determined. For comparison, the original weighting in tomoelastography, i.e., amplitude weighting, is also implemented. We evaluate these two weighting schemes in terms of three quality metrics, namely, estimation accuracy, SNR, and spatial resolution of the reconstructed wave speed maps. The simulation and experimental results for phantoms and a healthy human abdomen are provided.

2 | THEORY

In the multifrequency MRE technique, displacement fields of the tissues, u, are recorded by the aid of a dedicated MRI pulse sequence in each of the three Cartesian coordinates (index m) for different vibration frequencies (index n). This information is used for estimating elasticity distribution in the tissue of interest. Since in the body, the density of the tissue, ρ_0, is relatively constant and the shear modulus, μ, is related to the wave speed, c, by $\mu = c^2\rho_0$, while neglecting the viscous damping, the wave speed map can also be viewed as the elasticity map of the body.[22] Thus, in the tomoelastography technique, as a wave speed distribution of the tissue, $c\left(\vec{r}\right)$ is reconstructed and reported as one form of elasticity distribution assuming local homogeneity of the medium.

Considering the sum of plane waves in a local area, the displacement of the isochromat at position $\vec{r}$ can be expressed as:

$$u_{mn}\left(\vec{r}\right) = \sum_{l} u_{lmn}\left(\vec{r}\right). \tag{1}$$

Here, $\vec{r} = [x\,y]^T$ is the 2D position vector because implementation of tomoelastography is entirely slice-wise,[9] hence wave speed map for each slice is reconstructed separately. u_{lmn} represents a plane wave due to the actuator vibrating at frequency ω_n, recorded for the motion encoding direction, *m* ($m =$ 1,2 and 3 correspond to the x, y and z-directions, respectively), and in the propagation direction, *l*. Each of these plane waves can be written in phasor form as:

$$u_{lmn}\left(\vec{r}\right) = u_{0lmn}\left(\vec{r}\right)\exp\left(i\left(\vec{k}_{lmn}\left(\vec{r}\right)\cdot\vec{r} + \phi_{lmn}\left(\vec{r}\right)\right)\right), \tag{2}$$

where u_0 is the amplitude and ϕ is the phase of the plane wave.

Wavenumber $\vec{k}_{lmn}\left(\vec{r}\right)$ is a 2D vector at the spatial position $\vec{r}$. Its amplitude, $\|\vec{k}_{lmn}\left(\vec{r}\right)\| = k_{lmn}\left(\vec{r}\right)$, is equal to $\omega_n / c_{lmn}\left(\vec{r}\right)$, where $c_{lmn}\left(\vec{r}\right)$ is the wave speed. Note that $\vec{k}_{lmn}\left(\vec{r}\right)$ can be defined as a complex vector when considering the viscous damping.

The block diagram demonstrating the steps of tomoelastography inversion is depicted in Figure 1, and the details of the algorithm are explained in Tzschatzsch et al.[9]

As illustrated in the diagram, the input to this reconstruction technique is the amplitude-normalized complex-difference MRI signal $\exp(i\theta_{mn}(\vec{r},t))$. The first step is smoothing the complex signal by a 2D Gaussian kernel, $h_{GK}\left(\vec{r}\right)$, constructed in the image domain, followed by Laplacian based unwrapping[23] and harmonic selection using discrete Fourier transform (DFT) with N_t-points, which is equivalently the number of phase offsets acquired in the MRE experiment. To decompose superposed plane waves into plane waves propagating in different directions, directional filtering, $Z_l(\vec{k})$, is used. Note that directional filter ($Z_l(\vec{k})$) comprises a radial filtering component ($\beta(\vec{k})$) along with directional filtering, which eliminates longitudinal waves (Equations AP. 5 -AP. 6). Directional filters are constructed in k-space, where $\vec{k} = [k_x\,k_y]^T$ and k_x and k_y are the principal axes. Wavenumbers are obtained by computing the L_2-norm of the in-plane gradients of normalized displacement. Dividing the wavenumber by ω_n yields the inverse of the wave speed, $\hat{c}^{-1}$. In the final step, estimates of the inverse of wave speed for each wave direction (*l*), measurement direction (*m*), and frequency (*n*) as $\hat{c}_{lmn}^{-1}$ are combined using weighted summation as follows:

$$\hat{c}^{-1}\left(\vec{r}\right) = \sum_{lmn}\hat{c}_{lmn}^{-1}\left(\vec{r}\right)W_{lmn}\left(\vec{r}\right), \tag{3}$$

where

$$\hat{c}_{lmn}^{-1}\left(\vec{r}\right) = \frac{\hat{k}_{lmn}\left(\vec{r}\right)}{\omega_n}. \tag{4}$$

Here, the hat symbol (ˆ) indicates estimated values and that they are prone to errors due to incorrect measurements or approximations used in the mentioned algorithm. Furthermore, estimated wavenumber $\hat{k}_{lmn}\left(\vec{r}\right)$ and wave speed $\hat{c}_{lmn}\left(\vec{r}\right)$ are not vectors but only functions of the position since tomoelastography is concerned only with their magnitude due to isotropic medium assumption.

In the original tomoelastography reconstruction technique,[9] the multiple wave speed estimations, $\hat{c}_{lmn}$, are weight-averaged using:

$$W_{lmn}\left(\vec{r}\right) = \frac{\hat{u}_{0lmn}^4(r)}{\sum_{lmn}\hat{u}_{0lmn}^4(r)}. \tag{5}$$

In this method, using the fourth power of the local amplitude of the plane wave ensures that only wavenumbers constructed from high wave amplitudes will be averaged to compute the wave speed map.

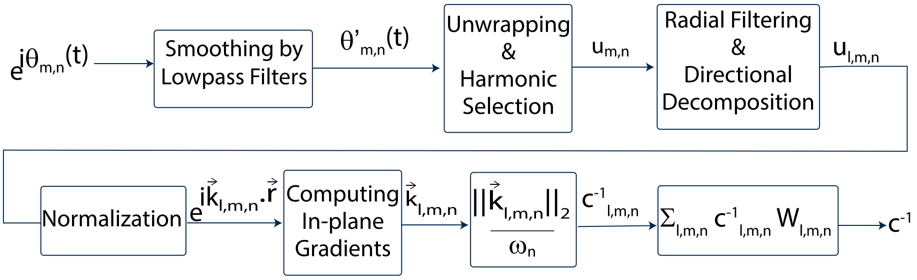

FIGURE 1 Block diagram of the original tomoelastography reconstruction. Amplitude-normalized complex-difference MRE images are the inputs of the reconstruction. In the last step of the reconstruction, weighted averaging is used to combine multiple estimations of the wave speed maps. The weights, W_{lmn}, in the original tomoelastography inversion are $\hat{u}_{0lmn}^4$

The alternative technique that we propose is SNR weighting. It can be shown that to maximize the SNR of the wave speed estimation, the square of individual SNRs of $\hat{c}_{lmn}^{-1}$, ${}^{c}\Psi_{lmn}$, should be used.[24] Here, we assume that the primary noise source on a complex MRI signal is thermal and modeled as additive white Gaussian noise (AWGN). With the high SNR assumption, the noise probability distribution remains Gaussian despite some nonlinear operations in the wave speed reconstruction algorithm. Thus, the mean and standard deviation (SD) of the noise probability distribution can be derived analytically from the tomoelastography inversion as (see Appendix for the derivation):

$${}^{c}\Psi_{lmn}\left(\vec{r}\right) = {}^{i}\Psi_{mn}\left(\vec{r}\right)\frac{\sqrt{N_t}}{\alpha}k_{lmn}\left(\vec{r}\right)u_{0lmn}\left(\vec{r}\right)\Delta \tag{6}$$

where α is

$$\alpha = \sqrt{\sum_{x=-N_x/2}^{N_x/2-1}\sum_{y=-N_y/2}^{N_y/2-1}\left(h_{GK}\left(\vec{r}\right)**\zeta_l\left(\vec{r}\right)\right)^2}, \tag{7}$$

and ${}^{i}\Psi_{mn}$ is the magnitude image SNR, N_x and N_y are the number of x and y pixels imaged, respectively, Δ is the isotropic in-plane resolution, $**$ is the 2D convolution operator, and $\zeta_l\left(\vec{r}\right)$ is the 2D inverse Fourier Transform of $Z_l(\vec{k})$.

However, due to the high SNR assumption in the derivation, SNR values at the output of the directional filters, ${}^{u}\Psi_{lmn}$, which do not satisfy the high SNR assumption, are thresholded prior to the weighting step by equating them to zero (i.e., set ${}^{c}\Psi_{lmn} = 0$ if ${}^{u}\Psi_{lmn}\left(\vec{r}\right) < {}^{thr}\Psi_{lmn}\left(\vec{r}\right)$). The SNR threshold, ${}^{thr}\Psi_{lmn}\left(\vec{r}\right)$, is determined by comparing the results of Monte Carlo computations to the analytical derivations. After thresholding, the SNR-weighted reconstruction weights are chosen as:

$$W_{lmn}\left(\vec{r}\right) = \frac{{}^{c}\Psi_{lmn}^{2}\left(\vec{r}\right)}{\sum_{lmn}{}^{c}\Psi_{lmn}^{2}\left(\vec{r}\right)}, \tag{8}$$

where

$${}^{u}\Psi_{lmn}\left(\vec{r}\right) = {}^{i}\Psi_{mn}\left(\vec{r}\right)\frac{u_{0lmn}\left(\vec{r}\right)\sqrt{N_t}}{\sqrt{2}\alpha}. \tag{9}$$

The required data and parameters to determine ${}^{c}\Psi_{lmn}\left(\vec{r}\right)$ in Equation (8) are given in Equation (6), which are image SNR ${}^{i}\Psi_{mn}\left(\vec{r}\right)$, number of phase offsets N_t, the energy of convolution of Gaussian kernel and the directional filter α, the wavenumber $k_{lmn}\left(\vec{r}\right)$, the filtered displacement $u_{0lmn}\left(\vec{r}\right)$ and the in-plane image voxel size Δ.

Note that the response of the directional filter, $Z_l(\vec{k}_{lmn})$, at the spatial position of the wavenumber on k-space, $\vec{k}_{lmn}$, is necessary for the SNR estimation. Here, we assume that the response of the directional filter is 1 if the wavenumber is in the range of the directional filter; otherwise, it is 0. In other words, $Z_l(\vec{k}_{lmn}) = 1$ if the l^{th} direction covers the propagation direction of the plane wave, which may not always be true but is designed to be very close to 1; otherwise, it is zero (see Appendix).

3 | METHODS

3.1 | Reconstructions

For wave speed reconstructions, tomoelastography inversion has been implemented for the proposed SNR weighting and the original amplitude weighting schemes, as explained in the previous section. To summarize regarding Equation (3), the original tomoelastography reconstruction uses $\hat{u}_{0lmn}{}^{4}$ as weights (i.e., amplitude-weighted as given in Equation (5)), and the SNR-weighted reconstruction uses ${}^{c}\Psi_{lmn}$ (as given in Equation (8)). Each SNR value (${}^{u}\Psi$ for each index and pixel) at the output of the direction filter (i.e., ${}^{u}\Psi$) is checked if it is greater than the threshold, which is determined by the minimum SNR (${}^{thr}\Psi$) that analytical derivations hold for. If ${}^{u}\Psi$ exceeds the threshold, the weight is set to the square of the SNR of c^{-1} (${}^{c}\Psi$); otherwise, ${}^{c}\Psi$ is set to zero.

3.2 | Simulations

MRE simulations are performed on four simulation phantoms (SPs). The displacement data for the first simulation phantom (SP#1) were generated via MATLAB (Burlington, MA, USA), whereas the second (SP#2), third (SP#3) and fourth (SP#4) simulation phantoms were generated via COMSOL

Multiphysics (COMSOL, Stockholm, Sweden) finite element method (FEM) software, as depicted in Figure 2A. Wave speed maps were reconstructed from the displacement data using MATLAB for all simulation phantoms.

In SP#1, a 2D plane wave simulation was generated in a homogeneous medium at a single frequency using MATLAB. The wave speed was 3.2 m/s, and the excitation frequency was swept from 30 to 72 Hz with 6 Hz increments. The resolution of SP#1 was 1.5 mm isotropic and size of the phantom is $15 \times 15\ cm^2$, hence 100×100 pixels. Zero padding was used to extend the data to 128×128 pixels, $192 \times 192\ mm^2$.

SP#2 was a square-shaped phantom with each side 20 cm long, consisting of two media with different wave speeds: 1.9 m/s for $y > 0$ and 2.5 m/s for $y \le 0$ (with the origin being the center of the phantom). Prescribed sinusoidal displacement with an amplitude of 5 μm in the x-direction was assigned to the top side, and frequency-domain analyses were performed for excitation frequencies of 30 to 72 Hz with 6 Hz increments. Complex displacement data in the x- and y-directions were exported with 1.5 mm isotropic resolution to be processed in MATLAB.

For SP#2, data were read in MATLAB and cropped to the middle $162\,mm \times 162\,mm$ square to decrease the effect of reflected waves in the inversion. Furthermore, zero padding was used to extend the region of interest to $189\,mm \times 189\,mm$ with the center square, $100\,mm \times 100\,mm$, being the phantom.

Additionally, to be convenient and use the same reconstructions used for the experimental data, the displacement fields in z-direction were taken as zero, since in the MRE experiments, the displacement fields are recorded in all three directions.

SP#3 was the same as SP#2 with two media having wave speeds of 1.75 and 3.5 m/s.

SP#4 was 3D, with three inclusions having different sizes and shear wave speeds. The diameters of the inclusions were 1.5, 2.5 and 3.5 cm, having shear wave speeds of 2.5, 3 and 2 m/s, respectively. The dimensions of the phantom were $20 \times 10 \times 8\ \text{cm}^3$ with resolution 1.5 mm isotropic and the shear wave speed for the background was 2.2 m/s. The excitation frequency was swept from 30 to 72 Hz with 6 Hz increments.

For SPs#2-4, the Poisson ratio (ν) and density (ρ) were assigned as 0.499 and 1040 kg/m^3, respectively. To account for damping in the models, complex Young's moduli were assigned as $E = 2(1+\nu)\rho c^2 + i0.05(2(1+\nu)\rho c^2)$, where c is the wave speed, as given for each phantom in Figure 2A.

Using COMSOL Multiphysics, MRE simulations were conducted on a 3D human abdomen model developed from Austin Man v2.4, with voxel size $2 \times 2 \times 2\ mm^3$.[25] The Poisson ratio, density and complex Young's moduli were assigned for the segmented tissues obtained from previous studies.[9,26-28] The assigned parameters are given in Supporting Information Table S1. Prescribed displacement was assigned to the surface of the anterior abdomen, and frequency domain analyses were performed, sweeping the excitation frequency from 30 to 48 Hz with 6 Hz increments. Complex displacement fields were exported with 2 mm isotropic voxels and then converted to eight phase-offset real displacement data. Then, simulated complex MRI signal data were constructed with unit magnitude and eight phase-offset real displacement data being the phase to be processed for wave speed map calculations using MATLAB. In addition, to evaluate the performance of the weighting schemes under noise, complex AWGN was added to the simulated complex MRI signal at different SNR levels in a reasonable range for each excitation frequency. The mean SNR level was 20, the minimum was 16 and the maximum was 24. Furthermore, 12 directional filters were employed for all of the data mentioned in this study.

Note that for all of the simulated MRE data when noise is not added, the image SNR (${}^{i}\Psi$) is assumed to be very high so that they cancel out in the normalization of the weighting. Thus, none of the weights are thresholded. However, this is called the no-noise case in this paper since noise is not added, but only a constant high SNR is assigned to the image SNR in Equation (6).

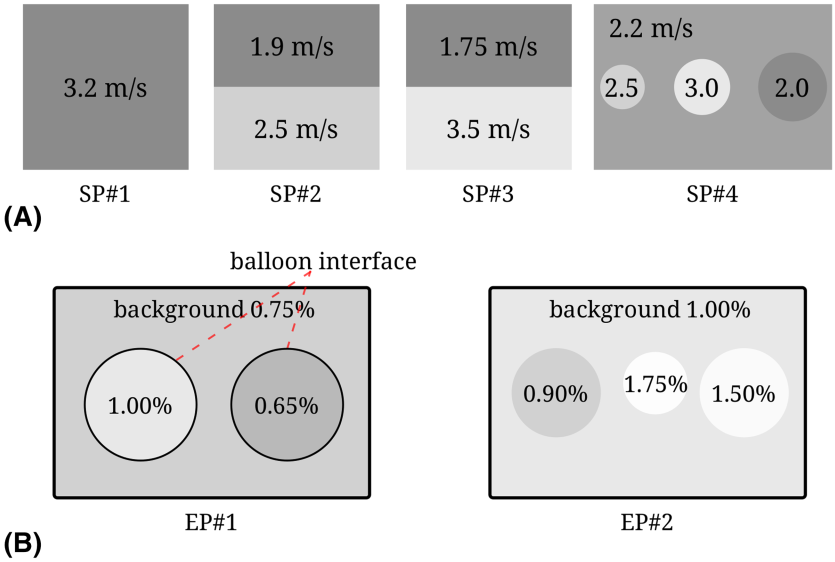

FIGURE 2 (A) Simulation phantoms depicting ground truth values for the real part of their wave speeds. (B) Experimental phantoms showing the agar-agar powder concentrations for the background and inclusions

3.3 | Validation of analytical SNR derivations and performance analyses

To validate the analytically derived SNR equation in Equation (8), MCS was conducted on single excitation frequency data (72 Hz) of SP#1. For a number of trials (N), chosen as 100, AWGN was added to the displacement data, followed by tomoelastography inversion. First, the mean and SD of wave speed maps were computed over N and then averaged over a region of interest (ROI) with size MxM (M=87 pixels). The SNR was obtained by the ratio of the 2D-averaged mean to the SD. In addition, the analytically approximated SNR values were compared with the SNR obtained by MCS. The noise level of AWGN was swept from SNR=0.5 to 10 with an incremental step of 0.1. The minimum SNR value that the high SNR assumption holds ($^{thr}\Psi$) for the analytical approximations was determined. Additionally, to analyze the effect of the assumption of the wave in a directional filter being fully present or fully absent, another simulation was performed. The angle of the plane wave was swept from 0^o to 360^o with 1^o increments when the image SNR was 5, and 12 directional filters were present.

The quality of the reconstructed wave speed maps was evaluated using three performance metrics. The first metric is the estimation error, in which the root mean square (RMS) error is computed for each reconstructed wave speed map with respect to the ground truth. This metric was computed for SPs#1-4.

The second metric is edge response analysis to investigate the resolution. This metric was only evaluated for SP#2 and SP#3. In the reconstructed wave speed maps, the number of pixels required for the transition between two mediums with different wave speeds was measured.

For the third metric, SNR performance, MCSs were conducted on SP#1. The number of trials was chosen as 50. The mean and SD were calculated over 50 trials and then averaged in an ROI of 87x87 pixels. The noise level of AWGN was swept from mean SNR=1 to 5 with 0.1 increments. Note that the "mean SNR" is the expected value of the SNRs of multifrequency displacement data since the SNR of the displacement data can be different at each frequency due to differences in MEG duration resulting in differences in TE and hence in SNR ($^{i}\Psi_{mn}$). Thus, we simulated this variation by letting the SNR levels of the complex AWGN vary by 20%.

3.4 | MRI experiments

MRE experiments were conducted on a Siemens TIM Trio 3 Tesla MRI scanner. A spin-echo echo-planar imaging (EPI-SE) pulse sequence with a trapezoidal motion encoding gradient (MEG) was used for acquisition. A single receive channel of the spine coil was used to record the signal. Data were collected for 8 excitation frequencies, 30 to 72 Hz, with 6 Hz increments. The sequence parameters were TR = 500 ms, TE = 82 ms ($\omega_1/2\pi = 30Hz$), TE = 71 ms ($\omega_2/2\pi = 36Hz$), TE = 70 ms ($\omega_{3,4,5,6,7,8}/2\pi = [42:6:72]Hz$), FOV = 240 mm x 180 mm, resolution = 2.5 x 2.5 x 2.5 mm^3, amplitude of MEG G_{MEG} = 20 mT/m, and number of MEGs N_{MEG} = 1. Five slices were acquired in each TR. Two acquisitions were made for each scan by switching the polarity of the zeroth- and first-moment nulled MEG, matched to the excitation frequency. Eight phase-offset data were collected for each excitation frequency.

The experimental phantoms (EPs) are shown in Figure 2B. EPs#1-2 were prepared from different concentrations of agar-agar powder (Agar-Agar Kobe I pulv., Roth, Karlsruhe, Germany), which were stirred in water and boiled for approximately 2 minutes.

For EP#1, agar-agar powder concentrations for the background, first and second inclusions were 0.75%, 1.00% and 0.65%, respectively. In EP#1, inclusions were injected inside balloons; hence, there were balloon interfaces between the inclusions and the background.

For EP#2, agar-agar powder concentrations for the background, first, second and third inclusions were 1.00%, 0.90%, 1.75% and 1.50%, respectively. There were no interfaces between inclusions and the background in EP#2. A box with dimensions of 19x15x10 cm^3 was used. A few drops of olive oil were applied to the inner surfaces of the box to allow the phantom to be removed easily without rupturing after solidification. Three rods with diameters of 3.5, 2 and 3.5 cm were placed vertically in the first, second and third inclusions, respectively. The background agar-agar water mixture was poured and allowed to solidify for 12 hours at room temperature. Then, each rod was removed, and each agar-agar powder water mixture was poured and allowed to solidify for half an hour, one by one. The whole phantom was allowed to solidify for another 12 hours at room temperature. An identical box side surface 19x15 cm^2 was cut. For the experiment, the phantom was placed inside the cut box and placed horizontally on the patient table in the MRI scanner, with the cut surface at the top. Hence, the phantom was excited by a plate, driven by a mechanical actuator, through the window opening of the cut box. Unless the phantom was placed in a box during the experiment, we observed deformation as multiple ruptures appeared on the phantom during the experiment. Hence, we decided to perform the experiments inside a box. Descriptive photographs showing the preparation steps of EP#2 are depicted in Supporting Information Figure S1.

Furthermore, multifrequency MRE displacement data of a human liver provided online on BIOQIC-Apps (Charité - Universitätsmedizin Berlin, Berlin, Germany)[29] were utilised in tomoelastography inversion using the mentioned weighting schemes. The excitation frequencies are 30, 40 and 50 Hz, with 2.7 mm in-plane resolution and 5 mm slice thickness.

For all experimental data, assuming a high SNR, noise on the phase was measured using the imaginary (or real) part of the noise measured on the background, inside a rectangular ROI with a size of 96x15 pixels for phantoms and 22x17 pixels for the human abdomen, of the complex MRI signal by averaging in the phase offset and direction of motion dimensions.

4 | RESULTS

4.1 | Simulation results

Validation of analytical SNR derivations using MCS: The MCS results to validate the SNR derivations are depicted in Figure 3. It can be observed that the analytical derivations hold for ${}^{i}\Psi_{mn}\left(\vec{r}\right) \geq 3$ since the ratio of the means and SDs becomes steady, and their deviations are approximately 1%. Hence, using Equation (9), the corresponding SNR threshold, ${}^{thr}\Psi_{lmn}\left(\vec{r}\right)$, was computed at the output of directional filters, equating low SNR weights to zero. In other words, ${}^{thr}\Psi_{lmn}\left(\vec{r}\right)$ is determined by setting ${}^{i}\Psi_{mn}\left(\vec{r}\right) = 3$ in Equation (9), which yields ${}^{thr}\Psi_{lmn}\left(\vec{r}\right) = 3u_{0lmn}\left(\vec{r}\right)\sqrt{N_t}/\left(\sqrt{2}\alpha\right)$. Figure 3C demonstrates that the SNR of the wave speed computed by MCS deviates from the analytical SNR when the wave propagation direction and direction of one of the directional filters do not exactly match. This deviation is due to our assumption in the derivation that a directional filter exactly matches to a wave or exactly misses it. Since we have used 12 directional filters for this simulation, the largest deviation occurs at multiples of 15^{o}, measured as 9%.

Estimation Error: The estimation accuracy values for the results of tomoelastography inversions using the two different weighting schemes were computed for SPs#1-4, measured by the RMS percentage error normalized to the ground truth. For the amplitude-weighted reconstruction, the normalized RMS errors were 2%, 4%, 6% and 5% for SPs#1, 2, 3 and 4, respectively. The same results were obtained for the SNR-weighted reconstruction, except for SP#2, for which the normalized RMS error was 3%. Wave speed maps, line profiles and mean±SD plots for SP#4 are depicted in Figure 4, in which no significant differences are observed between results of two weighting schemes.

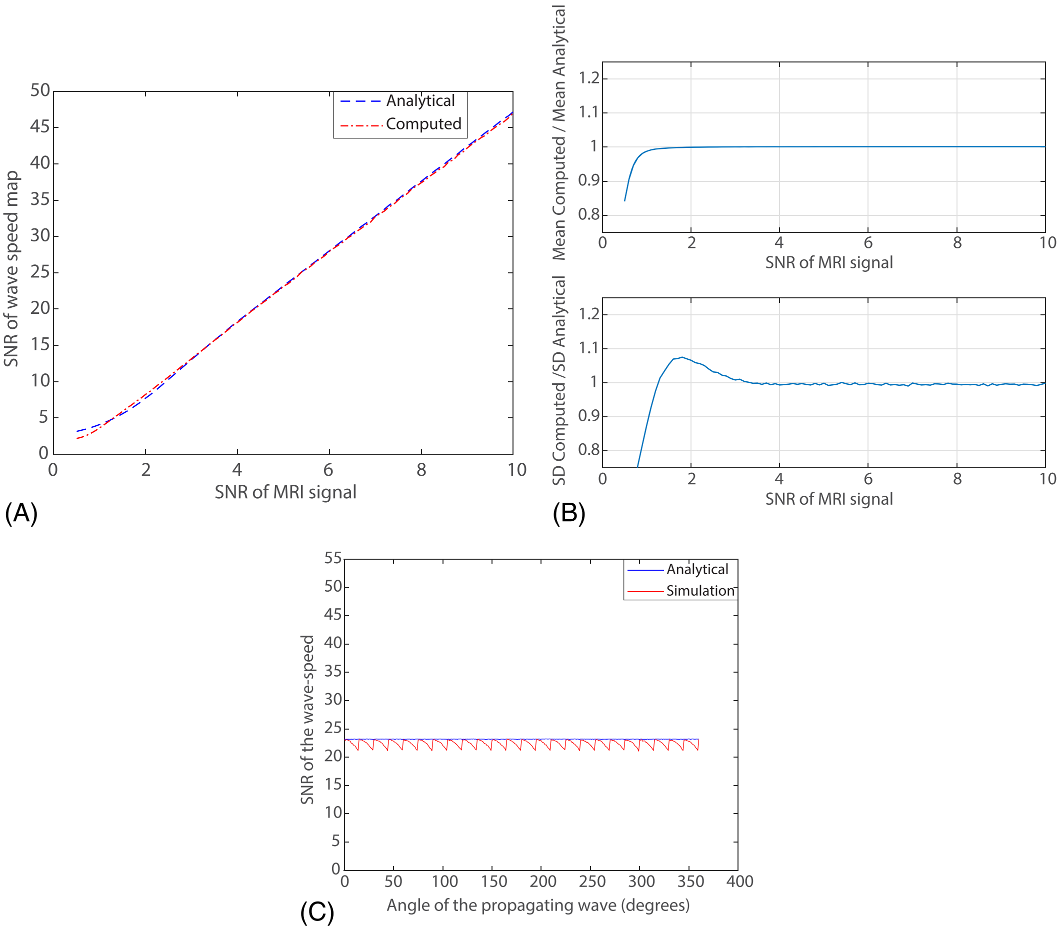

FIGURE 3 Validation of analytical approximations for the SNR by comparing it to the computed SNR using Monte Carlo simulations. (A) The SNR of the wave speed versus the SNR of the complex MRI signal for analytical and computed SNR values. (B) (Top) Ratio of the 2D-averaged mean of the wave speed reconstructed over 100 repetitions to the analytical mean wave speed at each image SNR. (Bottom) Ratio of the 2D-averaged SD of the wave speed reconstructed over 100 repetitions to the analytical SD of the wave speed at each image SNR. It can be observed that analytical derivations hold for ${}^{i}\Psi_{mn}\left(\vec{r}\right) \geq 3$ since the ratio of SDs becomes steady. (C) Comparison of analytical and MCS computed SNR, where the x-axis indicates the angle of the plane propagating in the x-y plane (i.e., $\arg\{\vec{k}\}$) when SNR=5, and 12 directional filters are present

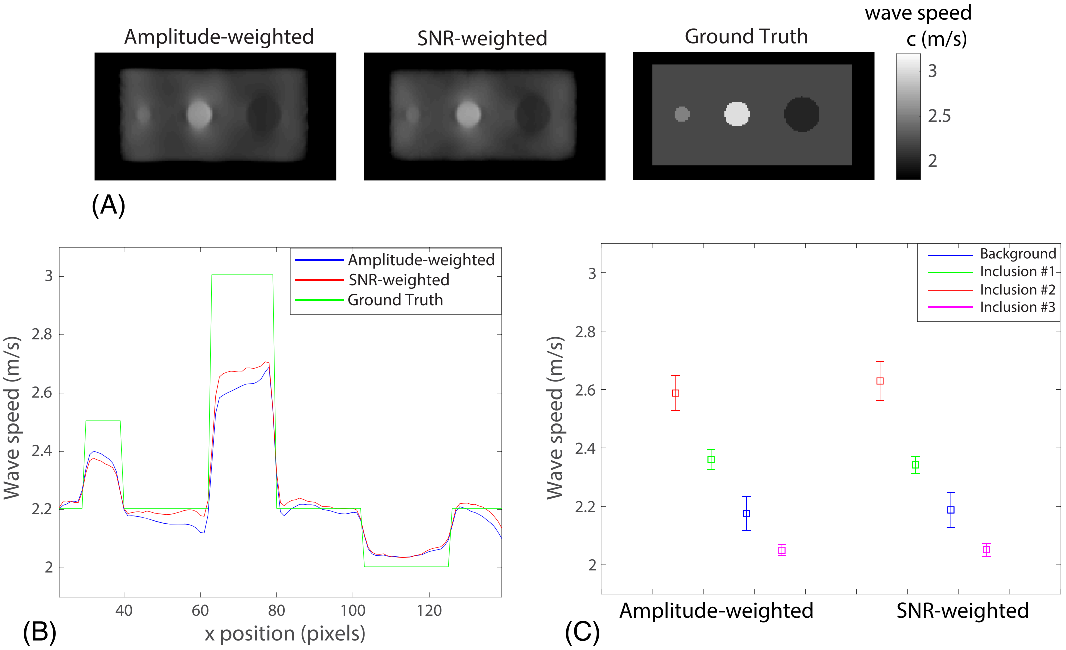

FIGURE 4 (A) Wave speed maps (B) line profiles for center horizontal line (C) mean±SD plots for each region for the two weighting schemes for SP#4. Assigned shear wave speed values are 2.2, 2.5, 3 and 2 m/s for background, inclusion #1-4, respectively

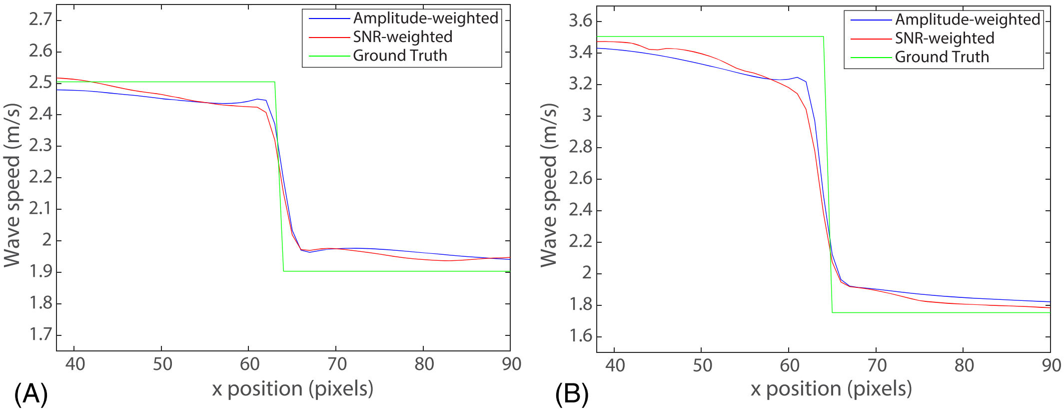

FIGURE 5 Wave speed values plotted for a cross-sectional line near the step between two mediums to analyze edge response for the two weighting schemes for (A) SP#2 and (B) SP#3

Edge Response Analysis: The edge responses on the center cross-sectional line of the reconstructed wave speed maps are illustrated for each weighting technique in Figure 5. The number of pixels required for the transition was measured to compare the resolution of the wave speed maps reconstructed using different weightings in tomoelastography inversion. The transition was quantified as 3 pixels for all reconstructions.

SNR Performance: The normalized mean and standard deviation versus mean SNR of complex MRI signal obtained by MCS is demonstrated in Figure 6. Note that the normalized mean and standard deviation imply that the computed mean and SD were divided by the ground truth wave speed value of 3.2 m/s. With a low SNR, there is 10% bias when the amplitude-weighted reconstruction has been used, whereas there is no bias when SNR weighting has been used. In addition, the normalized SD for the SNR-weighted reconstruction is lower than the normalized SD of the conventional weighting by a factor of two.

Abdomen MRE Simulations: Reconstructed wave speed maps are depicted in Figure 7 for the no-noise and AWGN-added cases and compared with the assigned wave speed values used in the simulation. For the no-noise case, the reconstructed wave speed maps are in good agreement with the ground truth wave speed map, except for some blurriness. For the noise-added case, it can be seen that the wave speed map reconstructed by conventional weighting suffers from noise, whereas the reconstructed wave speed map is slightly affected by noise when SNR weighting has been used.

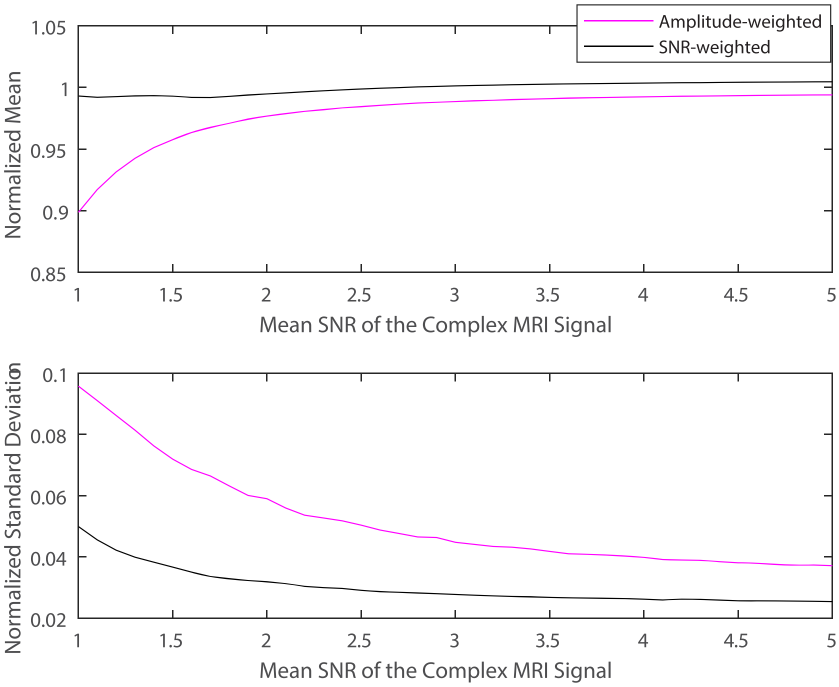

FIGURE 6 SNR performances computed by Monte Carlo simulations. 2D-averaged mean and standard deviation of wave speed maps, normalized to the ground truth wave speed, versus the image SNR

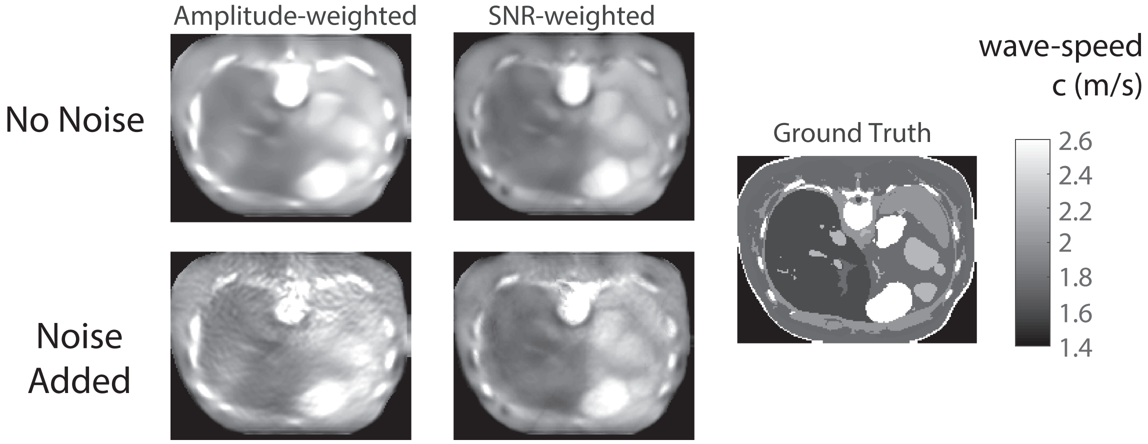

FIGURE 7 Reconstructed wave speed maps for the 3D healthy human abdomen model for the no-noise and noise-added case. The ground truth is also given, demonstrating the magnitude of the assigned wave speed distribution for the simulations

4.2 | Experimental results

The reconstructed wave speed maps for EP#1 are depicted in Figure 8A. Mean and SD of the measured wave speed values over the selected ROIs (Figure 8B) for EP#1 are demonstrated in Figure 8C. The second inclusion (0.65%) was expected to be softer than the background (0.75%); however, we can observe this result only for the SNR-weighted reconstruction, whereas in amplitude-weighted inversion, this difference cannot be differentiated well, as shown in Figure 8C. The amplitude-weighted reconstruction estimated the wave speed of the second inclusion (0.65%) to be greater than the background (0.75%) with a considerable deviation. It is also observed that, due to the interfaces of the balloons, which have short T_2s, around inclusions, the SNR-weighted reconstruction estimated a low wave speed.

The reconstructed wave speed results for each frequency, weights for each reconstruction and combined wave speed maps for EP#2 are shown in Figure 9. Mean and SD of the measured wave speed values over the selected ROIs for EP#2 are reported in Figure 10. The mean shear wave speed for the inclusion prepared with 1.75% agar-agar was measured to be greater than that of the inclusion prepared with 1.50% agar-agar only for the SNR-weighted inversion. Wave artifacts existing on the background of wave speed reconstruction using amplitude weights, as observed in Figure 9, resulted in greater wave speed deviations (Figure 10). To report quantitatively, mean and SD of the estimated wave speed for the background using amplitude weighted reconstruction is $2.93 \pm 0.31\ m/s$, whereas for SNR-weighted reconstruction mean and SD of the estimated wave speed is $3.00 \pm 0.22\ m/s$.

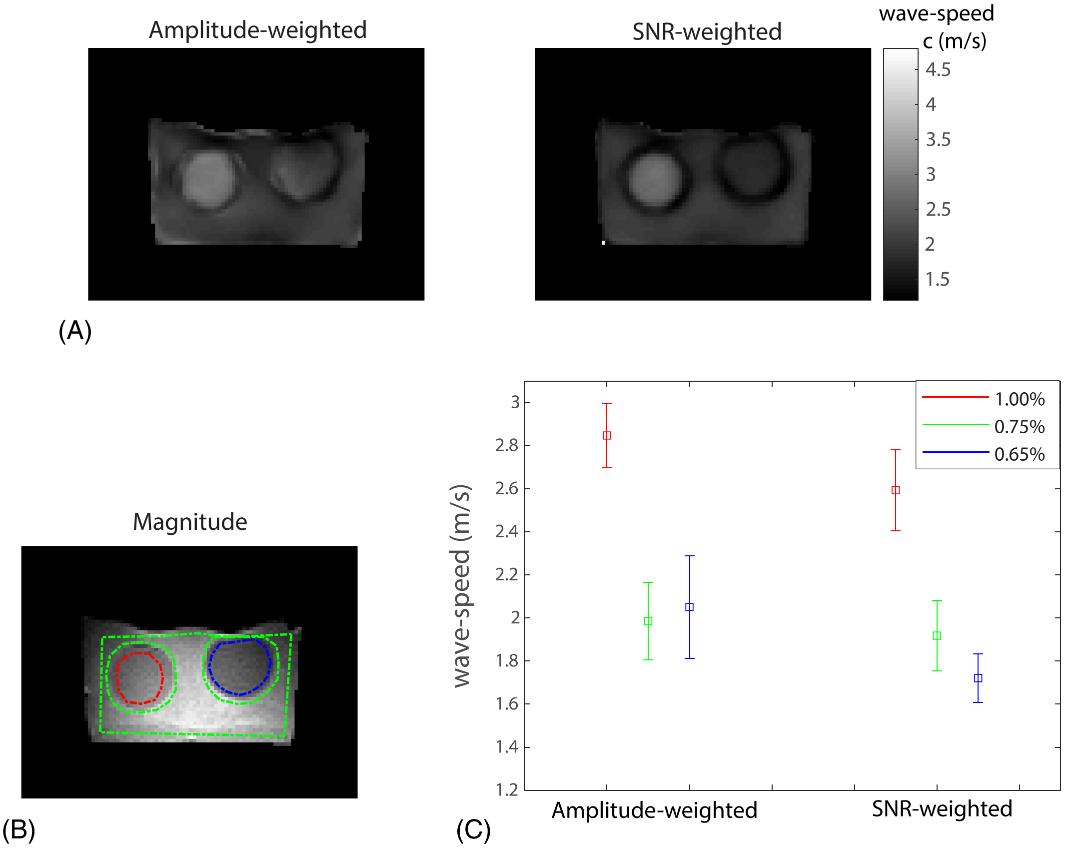

FIGURE 8 For EP#1 (A) Reconstructed wave speed maps (B) Selected ROIs for measuring wave speed values, depicted on the MRE magnitude image. The ROI for the background is selected as the region between the green curves. (C) Mean and SD values over the ROI, shown by squares and bars, respectively

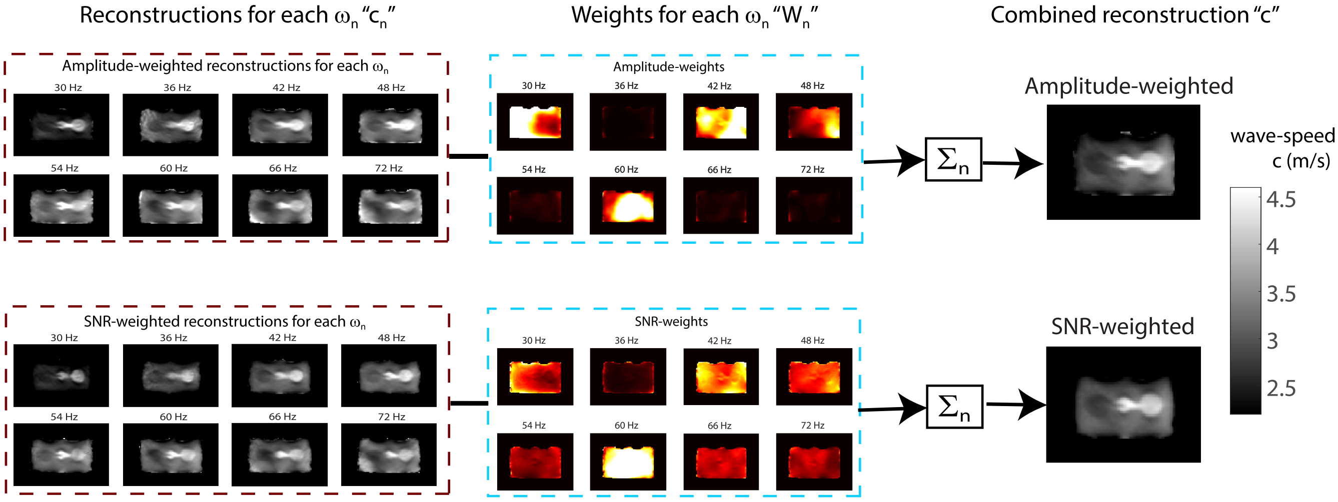

FIGURE 9 Reconstructed wave speed maps and weights for the two weighting schemes at each frequency in addition to the combined wave speed maps for EP#2

As observed in Figure 9, by comparing the two weighting schemes used in combining the reconstructed wave speed maps at different frequencies, it can be seen that amplitude weighting uses a single reconstruction result more heavily than others for each pixel, which is computed from the data that carry the maximum displacement and discards the other inversion results, because the fourth power of the magnitude of the displacement is used. On the other hand, SNR weighting uses more equally distributed weights.

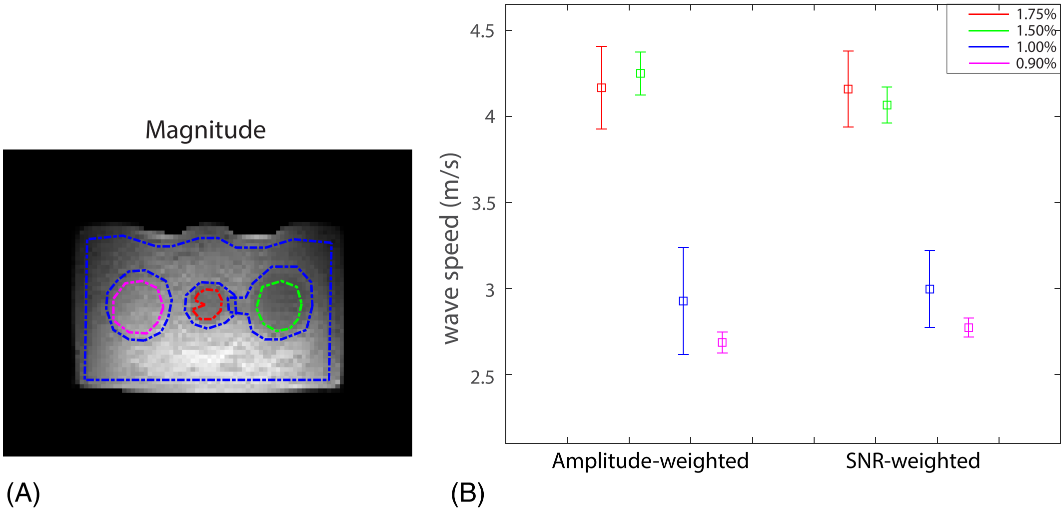

FIGURE 10 For EP#2 (A) Selected ROIs for measuring wave speed values, depicted on the MRE magnitude image. The ROI for the background is selected as the region between the blue curves. (B) Mean and SD values over the ROI, shown by squares and bars, respectively

Single frequency and combined wave speed maps for human liver are given in Figure 11A. To compare the computed wave speeds in the liver and spleen with previously reported values in the literature, wave speeds were measured in ROIs depicted on the magnitude image in Figure 11B. In the multifrequency result, for the liver, the mean and SD of the wave speeds were calculated as 1.68 ± 0.18 *m/s* and 1.54 ± 0.20 *m/s* for the amplitude-weighted and SNR-weighted reconstructions, respectively. For the spleen, the mean and SD of the wave speeds were calculated as 2.50 ± 0.23 *m/s* and 2.35 ± 0.21 *m/s* for the amplitude-weighted and SNR-weighted reconstructions, respectively.

5 | DISCUSSION

In this work, we have proposed a weighting scheme for combining multi-inversion data to maximize the SNR of the combined wave speed map. We evaluated the proposed reconstruction using three evaluation metrics, namely, estimation accuracy, spatial resolution and SNR performance.

The analytical SNR approximations are derived by assuming that the noise remains approximately Gaussian despite the nonlinear operations in tomoelastography inversion when the SNR is high enough. Hence, we determined the SNR threshold by comparing the SNR computed by MCSs and analytical approximations. It can be observed in Figure 3 that analytical approximations match with the MCS results for ${}^{i}\Psi_{mn}\left(\vec{r}\right) > 3$ (Figure 3). This result implies that the high SNR assumption used in the derivations fails below this value because the noise significantly deviates from Gaussian. Thresholding is necessary to eliminate the biased wave speed information reconstructed from these data. In addition, the MRE data having SNR below this value carry very little useful information, so they can be eliminated. The weighting schemes that are related to the amplitude of the displacement can be improved by using thresholding. Using the fourth power of the displacement eliminates the low displacement data because it is similar to choosing only the data with the highest displacement value, in a way thresholds the low displacement data, but this method also excludes useful data. Previously, to eliminate biased results from elasticity ROI measurements, various researchers reported wave-speed or shear modulus values in ROIs by masking them with a phase-difference SNR threshold.[30,31] Here, we are thresholding prior to combining multiple wave-speed maps, where SNR threshold has been determined by MCs. Furthermore, SNR estimates are used for weighting to combine multi-inversion results.

Additionally, analytical approximations for SNR are derived for assuming local homogeneity of the MRE magnitude image. For instance, SNR approximations may fail for the regions of tissues with rapid T_2 changes if a T_2-weighted EPI-SE pulse sequence is used, which is a common pulse sequence used in MRE imaging. The underestimation of wave speeds at the balloon interfaces, observed in Figure 8, might be due to the assumption of slow variation in the magnitude of the MRI signal spatially in the analytical approximation of the SNR.

Another assumption in the SNR derivations is that the response of the directional filter is set to 1 if the wavenumber is in the range of the directional filter; otherwise, it is set to 0. However, the filter response is not equal to 1 when there is some angle between the direction of the wavenumber and the directional filter while the wavenumber is still in the range of the filter. In Figure 3C, it is observed that the analytical SNR deviates from the MCS-computed SNR by 7% at most when twelve directional filters are present and the image SNR is 5.

Furthermore, analytical SNR approximations are derived for a single channel receive coil. When phased array coils are used, the method of obtaining the phase information requires additional nonlinear techniques.[32] One possible solution for this problem is to process each channel

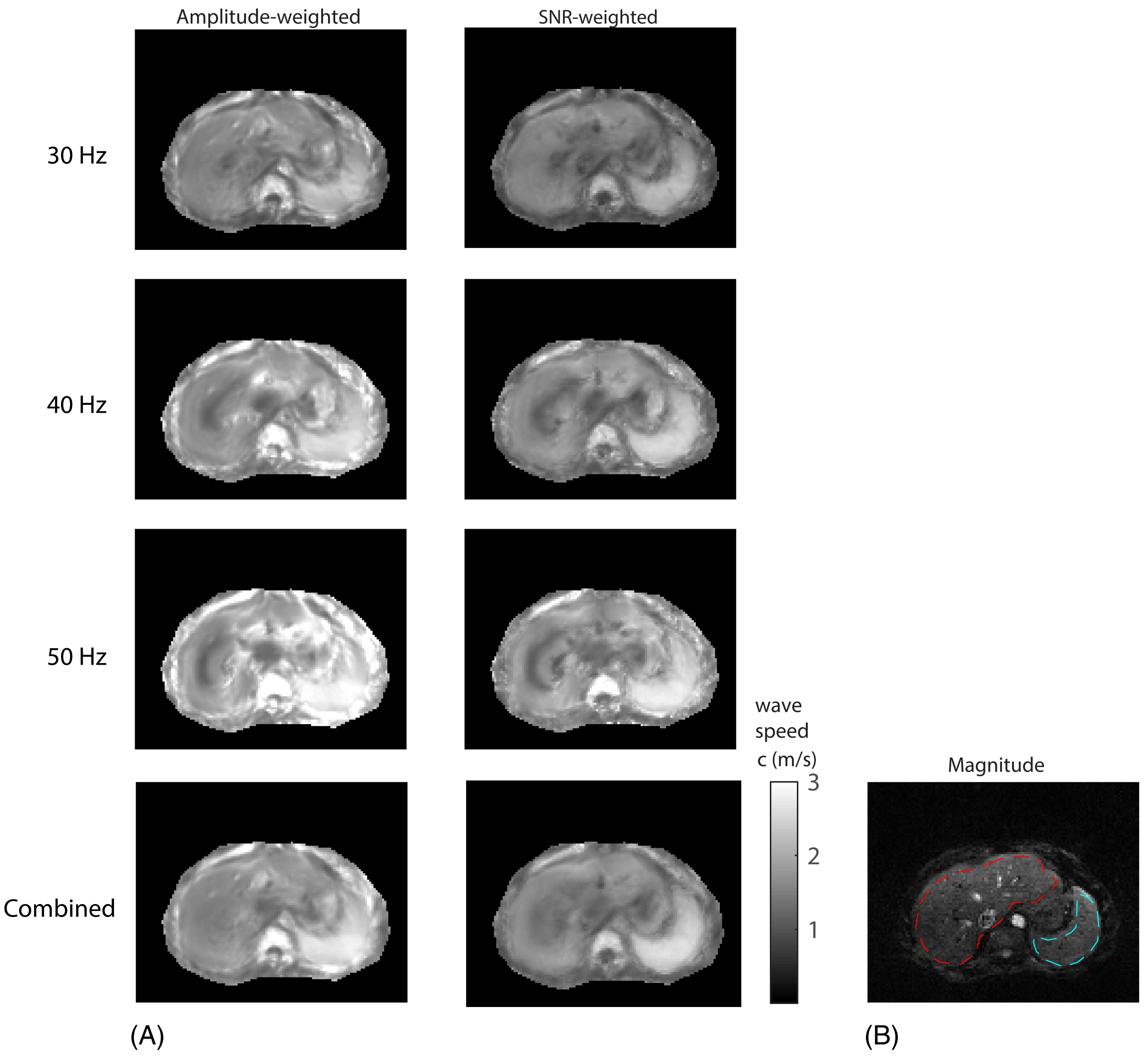

FIGURE 11 (A) Single frequency and combined multifrequency results for wave speed maps for MRE abdomen data. (B) Anatomical ROIs (liver (red) and spleen (blue)), selected on the MRE magnitude image, for measuring the mean and SD of the estimated shear wave speeds

information separately. In this case, the determined threshold will still be valid. However, when phase information is obtained from the combined image, a similar analysis must be carried out to understand the effect of these nonlinear techniques on the estimation of the wave speed.

Viscous damping distribution has not been reconstructed in this study. Usually, complex shear modulus is reported in MRE,[33-36] where the real part is the storage modulus related to elastic properties of the tissue and the imaginary part is the loss modulus related to viscous properties of the tissue. To compute viscous damping distribution $\vec{k}$ can be defined as a complex vector while assuming spatially constant wave amplitudes for u_{0lmn}, as formulated in Tzschatzsch et al.[9]

No differences are observed for the estimation accuracies and spatial resolutions of the proposed and conventional weighting schemes, and all of them are in good agreement with the ground truths; however, SNR performance analyses demonstrated that no bias occurred, and the SNR of the wave speed map was improved twofold when SNR weights were used instead of amplitude weights. Therefore, the proposed SNR weighting reconstruction significantly improved the SNR of the final wave speed map while achieving the same performance for the accuracy and spatial resolution compared to that of the conventional reconstruction. Similarly, probably due to noise, amplitude-weighted reconstruction could not have differentiated the wave speed alterations in EPs#1-2, whereas SNR-weighted reconstruction yielded the expected wave speed results, as observed in Figures 8-9.

It is not possible to directly compare the method and results in Tzschatzsch et al[9] because of differences in the implementations of Gaussian smoothing and directional filtering. For instance, the standard deviation of the Gaussian kernel is 2.75 mm in Tzschatzsch et al[9]; however, it is 2.16 mm for the in-vivo liver here. Hence, smoothing is slightly less in this study. Also, the compositions of directional filters are different. The directional filter's radial component is a ramp filter in Tzschatzsch et al.[9] We utilized the directional filter in the Equations AP. 5 -AP. 6 to eliminate the black stripe artifacts at organ boundaries, as reported in Tzschatzsch et al.[9] due to directional filters.

Regarding Figure 7, the blurriness of reconstructed wave speed maps for both weighting schemes is because of the number of directional filters in tomoelastography reconstruction since increasing the number of directional filters decreases the spatial resolution. For the noise-added case, we can observe that the amplitude-weighted inversion result has been severely affected by noise, whereas the SNR-weighted inversion result has been slightly affected.

In this study, MMRE displacement data for a healthy human abdomen FEM model have been introduced for the first time. The community can also benefit from this model to evaluate their inversion techniques for liver and spleen MRE.

For all experimental phantoms, the wave speeds measured were approximately 30% lower than the values observed by Hamhaber et al,[37] in which the same agar-agar powder had been used. The difference could be the result of using tap water instead of distilled water. Furthermore, the number of motion-encoding directions, excitation frequencies and inversion techniques are different.

The mean wave speeds of the liver and spleen were found to be consistent with the values reported in the literature.[9,26] Since in-vivo data have a good SNR at the level of 15 approximately, we do not expect any biased results due to noise. In a good SNR level, amplitude-weighted and SNR-weighted reconstruction should yield similar results, slightly lower or higher than each other, which is also the case here.

When single frequency in-vivo results are analyzed, it is observed that SNR-weighted wave-speed maps are more invariant to excitation frequency used compared to amplitude-weighted results. Low elasticity regions present in the center of the liver in SNR-weighted wave speed map in Figure 11, could be due to elasticity variations in some anatomical details such as blood vessels; however, it is not possible to know the exact reason of this lower elasticity since ground truth for in-vivo data is absent. As future work, to understand such elasticity variations in the SNR-weighted reconstruction, an extended in-vivo study has to be performed on a sufficient number of healthy and unhealthy subjects having age and sex diversity. For this study, despite the absence of a ground truth for the human liver results, based on significant improvements in the SNR of the elastography maps without any loss in resolution and accuracy, one may argue that SNR weighting is useful for MRE inversion.

Inspecting the derived SNR characteristic of the estimated wave speed (${}^{c}\Psi_{lmn}\left(\vec{r}\right)$) in Equation (6), it can be seen that most of the parameters are the same spatially and for weighting indices. The parameters that are not constant are the image SNR, the magnitude of the wavenumber and the amplitude of the displacement. The image SNR may vary spatially, most likely due to variation in the magnitude of the signal or through indices if the imaging parameters differ between scans such as TE. Since the SNR depends on the wavenumber, SNR weighting will favor reconstruction from the lowest excitation frequency among the same wave speed information obtained for the same spatial position if we assume that all the other parameters in Equation (6) are constant. If we assume that all the parameters except the amplitude of the filtered displacement are constant, then SNR weighting becomes equal to weighting with the square of the amplitude of the displacement with thresholding. To summarize, the proposed method both benefits from weighting with square of SNR and thresholding. For combining wave speed maps with the noise distribution of Gaussian, the optimum weighting for maximum SNR is to use square of SNR.[24] However, for low SNR cases, the noise distribution is not Gaussian; hence estimated SNR is incorrect due to Gaussian noise assumption in the derivations; therefore, thresholding is essential. To demonstrate the effect of thresholding, reconstructed wave speed maps using SNR weights with thresholding and without thresholding for noisy abdomen MRE simulation data have been demonstrated in Supporting Information Figure S2. It is observed that without thresholding reconstructed map is is biased in the regions with higher wave speed values.

The proposed weighting scheme may be more advantageous when there are SNR variations in the collected data because due to the image SNR term in Equation (6), improvement in the SNR performance becomes more significant than that in the original weighting scheme. Note that even though the noise level is the same throughout the experiment, the signal level may differ. For example, to collect MRE data at various excitation frequencies, the TE is varied to match it to the excitation frequency unless fractional encoding[38]is used.

When multidirectional and multifrequency data are acquired, the methods developed in this study may be applicable to reconstructions other than tomoelastography, such as Helmholtz's inversion,[5-7]multifrequency dual elasto visco inversion,[8] nonlinear inversion)[3,4] and multi-model direct inversion.[10] Note that the SNR-weighted reconstruction requires derivation of the analytical noise statistics. In this work, we have performed this derivation for tomoelastography. For other inversion algorithms, noise statistics must be rederived for the implementation of SNR weighting. Even reconstructions using amplitude-based weighting schemes such as using the first order, second order or energy of the displacement can benefit from employing thresholding.

Another idea could have been using strain weighting instead of amplitude weighting to eliminate cases of low elastic strain because the strain is directly related to the shear; hence, the magnitude of the shear strain produced by motion is more essential than the magnitude of the shear wave displacement. In fact, McGarry et al[18] showed in their nonlinear inversion method for elasticity reconstruction that strain-SNR measured by the octahedral shear strain (OSS)-SNR is more useful than motion-SNR to determine the reliability of the reconstructed elastogram from the displacement data. Improvements in the elasticity map were demonstrated in[17,39] when OSS was used for strain weighting in tomoelastography and Helmholtz inversion. Notably, OSS weighting is successful at interfaces and boundaries, which is expected because it uses strain weighting, so the reconstructed wave speed that is computed from the data with greater displacement jumps is weighted more, similar to slip-interface imaging.[40]

Moreover, this analysis is consistent with the conclusion of Manduca et al[19] since they suggested evaluating the reliability of the elasticity map generated depending on the number of derivatives used based on the number of derivatives in the SNR metric. For instance, it is recommended to use OSS-SNR[18] for the inversion methods consisting of only the first derivative and Laplacian-SNR for the reconstructions using the second derivative of the displacement field.

Furthermore, we have investigated the SNR characteristics of an MMRE inversion for the first time. The SNR derivations that we have developed in this study provide a useful tool for researchers to investigate the sensitivity of the SNR of the final wave speed map to the various parameters of the reconstruction technique, namely, tomoelastography. For example, one may investigate the sensitivity to the number of phase offsets and filter parameters.

6 | CONCLUSION

A new weighting scheme for combining multi-inversion reconstructions to maximize the SNR of the final wave speed map in tomoelastography has been proposed. The performance of the proposed weighting scheme is compared with that of the conventional amplitude-based method by using three performance measures, namely, the estimation error, spatial resolution and SNR of the final wave speed maps. SNR weighting significantly improved the SNR performance of the wave speed map while achieving the same performance for accuracy and spatial resolution. In addition, bias in the wave speed map has been eliminated in the low SNR case using the SNR weighting reconstruction.

ORCID

Cemre Ariyurek https://orcid.org/0000-0002-1691-7097
Bilal Tasdelen https://orcid.org/0000-0001-6462-3651
Yusuf Ziya Ider https://orcid.org/0000-0002-1961-6804
Ergin Atalar https://orcid.org/0000-0002-6874-6103

REFERENCES

1. Muthupillai R, Lomas DJ, Rossman PJ, Greenleaf JF, Manduca A, Ehman RL. Magnetic resonance elastography by direct visualization of propagating acoustic strain waves. *Science*. 1995;269(5232):1854–1857.
2. Manduca A, Muthupillai R, Rossman PJ, Greenleaf JF, Ehman RL. Image processing for magnetic-resonance elastography. In: Medical imaging 1996: Image processing, Vol. 2710 International Society for Optics and Photonics; 1996:616–624.
3. Van Houten EE, Miga MI, Weaver JB, Kennedy FE, Paulsen KD. Three-dimensional subzone-based reconstruction algorithm for mr elastography. *Magn Res Med Official J Int Soc Magn Res Med*. 2001;45(5):827–837.
4. Van Houten EE, Doyley MM, Kennedy FE, Weaver JB, Paulsen KD. Initial in vivo experience with steady-state subzone-based mr elastography of the human breast. *J Magn Res Imag*. 2003;17(1):72–85.
5. Manduca A, Lake DS, Kruse SA, Ehman RL. Spatio-temporal directional filtering for improved inversion of mr elastography images. *Med Image Anal*. 2003;7(4):465–473.
6. Papazoglou S, Hamhaber U, Braun J, Sack I. Algebraic helmholtz inversion in planar magnetic resonance elastography. *Phys Med Biol*. 2008;53(12):3147.
7. Hirsch S, Guo J, Reiter R, et al. Mr elastography of the liver and the spleen using a piezoelectric driver, single-shot wave-field acquisition, and multifrequency dual parameter reconstruction. *Magn Reson Med*. 2014;71(1):267–277.
8. Papazoglou S, Hirsch S, Braun J, Sack I. Multifrequency inversion in magnetic resonance elastography. *Phys Med Biol*. 2012;57(8):2329.
9. Tzschätzsch H, Guo J, Dittmann F, et al. Tomoelastography by multifrequency wave number recovery from time-harmonic propagating shear waves. *Med Image Anal*. 2016;30:1–10.
10. Silva AM, Grimm RC, Glaser KJ, et al. Magnetic resonance elastography: evaluation of new inversion algorithm and quantitative analysis method. *Abdom Imaging*. 2015;40(4):810–817.
11. Murphy MC, Manduca A, Trzasko JD, Glaser KJ, Huston III J, Ehman RL. Artificial neural networks for stiffness estimation in magnetic resonance elastography. *Magn Res Med*. 2018;80(1):351–360.
12. Barnhill E, Davies PJ, Ariyurek C, Fehlner A, Braun J, Sack I. Heterogeneous multifrequency direct inversion (hmdi) for magnetic resonance elastography with application to a clinical brain exam. *Med Image Anal*. 2018;46:180–188.
13. Bertalan G, Guo J, Tzschätzsch H, et al. Fast tomoelastography of the mouse brain by multifrequency single-shot mr elastography. *Magn Res Med*. 2019;81(4):2676–2687.
14. Klatt D, Hamhaber U, Asbach P, Braun J, Sack I. Noninvasive assessment of the rheological behavior of human organs using multifrequency mr elastography: a study of brain and liver viscoelasticity. *Phys Med Biol*. 2007;52(24):7281.
15. Parker KJ, Doyley MM, Rubens DJ. Imaging the elastic properties of tissue: the 20 year perspective. *Phys Med Biol*. 2010;56(1):R1.
16. Kalra P, Raterman B, Mo X, Kolipaka A. Magnetic resonance elastography of brain: Comparison between anisotropic and isotropic stiffness and its correlation to age. *Magn Res Med*. 2019;82(2):671–679.
17. Ariyurek C, Tasdelen B, Sadeghi-Tarakameh A, Ider YZ, Atalar E. Analysis and maximization of snr in mr elastography inversion. In: Proceedings of the 27th Annual Meeting of ISMRM, Montréal, Canada; 2019:3962.
18. McGarry MDJ, Van Houten EEW, Perrinez PR, Pattison AJ, Weaver JB, Paulsen KD. An octahedral shear strain-based measure of snr for 3d mr elastography. *Phys Med Biol*. 2011;56(13):N153.
19. Manduca A, Lake DS, Huynh KT, Eon RS, Annoni EM, Ehman RL. Consistent snr measures for magnetic resonance elastography. In: Proceedings of the 23rd Annual Meeting of ISMRM, Toronto; 2015:2519.
20. Johnson CL, Holtrop JL, McGarry MDJ, et al. 3d multislab, multishot acquisition for fast, whole-brain mr elastography with high signal-to-noise efficiency. *Magn Res Med*. 2014;71(2):477–485.
21. Guenthner C, Kozerke S. Encoding and readout strategies in magnetic resonance elastography. *NMR Biomed*. 2018;31(10):e3919.

22. Manduca A, Oliphant TE, Dresner MA, et al. Magnetic resonance elastography: non-invasive mapping of tissue elasticity. *Med Image Anal*. 2001;5(4): 237–254.
23. Dittmann F, Hirsch S, Tzschätzsch H, Guo J, Braun J, Sack I. In vivo wideband multifrequency mr elastography of the human brain and liver. *Magn Res Med*. 2016;76(4):1116–1126.
24. Unser M, Eden M. Weighted averaging of a set of noisy images for maximum signal-to-noise ratio. *IEEE Trans Acoust Speech Sig Process*. 1990;38(5): 890–895.
25. Massey JW, Yilmaz AE. Austinman and austinwoman: High-fidelity, anatomical voxel models developed from the vhp color images. In: 2016 38th Annual International Conference of the IEEE Engineering in Medicine and Biology Society (EMBC) IEEE; 2016:3346–3349.
26. Dittmann F, Tzschätzsch H, Hirsch S, et al. Tomoelastography of the abdomen: Tissue mechanical properties of the liver, spleen, kidney, and pancreas from single mr elastography scans at different hydration states. *Magn Res Med*. 2017;78(3):976–983.
27. Mariappan YK, Glaser KJ, Ehman RL. Magnetic resonance elastography: a review. *Clinic Anatom*. 2010;23(5):497–511.
28. Kolipaka A, Woodrum D, Araoz PA, Ehman RL. Mr elastography of the in vivo abdominal aorta: a feasibility study for comparing aortic stiffness between hypertensives and normotensives. *J Magn Res Imaging*. 2012;35(3):582–586.
29. MMRE liver data. BIOQIC apps website. Published November 06, 2018. https://bioqic-apps.charite.de/downloads; 2018.
30. Kruse SA, Rose GH, Glaser KJ, et al. Magnetic resonance elastography of the brain. *Neuroimage*. 2008;39(1):231–237.
31. Yin M, Talwalkar JA, Glaser KJ, et al. Dynamic postprandial hepatic stiffness augmentation assessed with mr elastography in patients with chronic liver disease. *Amer J Roentgenol*. 2011;197(1):64–70.
32. Constantinides CD, Atalar E, McVeigh ER. Signal-to-noise measurements in magnitude images from nmr phased arrays. *Magn Res Med*. 1997;38(5): 852–857.
33. Green MA, Bilston LE, Sinkus R. In vivo brain viscoelastic properties measured by magnetic resonance elastography. *NMR Biomed Intern J Devoted Develop Appl Magn Res Vivo*. 2008;21(7):755–764.
34. Klatt D, Papazoglou S, Braun J, Sack I. Viscoelasticity-based mr elastography of skeletal muscle. *Phys Med Biol*. 2010;55(21):6445.
35. Fovargue D, Kozerke S, Sinkus R, Nordsletten D. Robust mr elastography stiffness quantification using a localized divergence free finite element reconstruction. *Med Image Anal*. 2018;44:126–142.
36. Clayton EH, Garbow JR, Bayly PV. Frequency-dependent viscoelastic parameters of mouse brain tissue estimated by mr elastography. *Phys Med Biol*. 2011;56(8):2391.
37. Hamhaber U, Grieshaber FA, Nagel JH, Klose U. Comparison of quantitative shear wave mr-elastography with mechanical compression tests. *Magn Res Med Official J Int Soc Magn Res Med*. 2003;49(1):71–77.
38. Rump J, Klatt D, Braun J, Warmuth C, Sack I. Fractional encoding of harmonic motions in mr elastography. *Magn Res Med Official J Int Soc Magn Res Med*. 2007;57(2):388–395.
39. Ariyurek C, Tasdelen B, Barnhill E, Ergun AS, Ider YZ, Atalar E. Usage of octahedral shear strain weights in the inversion of multifrequency mr elastography. In: Proceedings of the 26th Annual Meeting of ISMRM, Paris, France; 2018:1076.
40. Yin Z, Glaser KJ, Manduca A, et al. Slip interface imaging predicts tumor-brain adhesion in vestibular schwannomas. *Radiology*. 2015;277(2):507–517.
41. Bernstein MA, Ikezaki Y. Comparison of phase-difference and complex-difference processing in phase-contrast mr angiography. *J Magn Res Imaging*. 1991;1(6):725–729.

SUPPORTING INFORMATION

Additional supporting information may be found online in the Supporting Information section at the end of this article.

How to cite this article: Ariyurek C, Tasdelen B, Ider YZ, Atalar E. SNR Weighting for Shear Wave Speed Reconstruction in Tomoelastography. *NMR in Biomedicine*. 2021;34:e4413. https://doi.org/10.1002/nbm.4413

APPENDIX A

The actual complex-difference MRI signal is $S_{mn}(\vec{r},t)=A_{mn}\left(\vec{r}\right)\exp(i\theta_{mn}(\vec{r},t))$, obtained from two measurements with opposite motion encoding gradient (MEG) polarity, where A is the magnitude and θ is the phase of the noiseless complex signal. The primary noise source on a complex MRI signal is thermal and is modeled as additive white Gaussian noise (AWGN), and the same applies to a complex-difference MRI signal[41]; hence, let the measured complex-difference MRI signal be denoted as $\hat{S}$ and the SNR of $|\hat{S}|$ be ${}^{i}\Psi$. Complex MR images are reconstructed by taking the 2D Fourier transform of the complex MRI signal.

In MRE, we are interested in the phase since motion is encoded in the phase, equivalent to:

$$\theta_{mn}(\vec{r},t)=\sum_{l}u_{0lmn}\left(\vec{r}\right)\cos\left(\vec{k}_{mn}\left(\vec{r}\right)\cdot\vec{r}-\omega_{n}t+\phi_{mn}\left(\vec{r}\right)\right) \tag{AP.1}$$

For a high SNR (i.e. ${}^{i}\Psi > >1$), noise distribution in the phase can be approximated to be equal to noise distribution in the real or imaginary part of the complex MRI signal, hence expected value (E[]), and standard deviation (SD[]) of the phase are given as:

$$E[\arg\{S_{mn}(\vec{r},t)\}] = \theta_{mn}(\vec{r},t) \tag{AP.2}$$

and

$$SD[\arg\{S_{mn}(\vec{r},t)\}] = \frac{1}{{}^{i}\Psi_{mn}\left(\vec{r}\right)}, \tag{AP.3}$$

respectively. Here, arg returns angle of the complex number.

Now, we follow tomoelastography inversion step by step, as described in Tzschatzsch et al.[9] The first step of the inversion is smoothing the complex signal $\exp(i\hat{\theta})$ by lowpass filtering using a 2D Gaussian kernel, $h_{GK}\left(\vec{r}\right)$, having a standard deviation of $\sigma_{GK} = 0.8$ pixels and size 5×5 pixels, constructed in the image domain as:

$$h_{GK}\left(\vec{r}\right) = \frac{\exp(-r^2/2\sigma_{GK}^2)}{\sum_{x=-2}^{2}\sum_{y=-2}^{2}\exp(-r^2/2\sigma_{GK}^2)}, \tag{AP.4}$$

which does not alter the mean since it has unit DC gain $\left(\text{i.e.,} \sum_{x=-\infty}^{\infty}\sum_{y=-\infty}^{\infty} h_{GK}\left(\vec{r}\right) = 1\right)$. Hence, $E[\hat{\theta}'_{mn}(\vec{r},t)] = E[\arg\{S_{mn}(\vec{r},t)\}]$, and the SD of the smoothed phase becomes:

$$SD[\hat{\theta}'_{mn}(\vec{r},t)] = \frac{1}{{}^{i}\Psi_{mn}(\vec{r})} \underbrace{\sqrt{\sum_{x=-2}^{2}\sum_{y=-2}^{2}(h_{GK}(\vec{r}))^2}}_{\text{Smoothing}} \tag{AP. 5}$$

We assume that the Gaussian kernel Equation (AP. 4), used in smoothing, is a very light filter, which has an effect only on the noise characteristics. Additionally, $A_{mn}\left(\vec{r}\right)$ is assumed to be locally homogeneous, which is not true at the edges of the tissue.

Smoothing is followed by unwrapping and harmonic frequency selection:

$$E[Re\{\hat{u}_{mn}(\vec{r})\}] = \sum_{l} u_{0lmn}(\vec{r}) \underbrace{\frac{N_t}{2} Re\{\exp(-i(\vec{k}_{mn}(\vec{r})\cdot\vec{r} + \phi_{mn}(\vec{r})))\}}_{\substack{\text{Harmonic}\\ \text{Frequency}\\ \text{Selection}}} \tag{AP. 6}$$

$$E[Im\{\hat{u}_{mn}(\vec{r})\}] = \sum_{l} u_{0lmn}(\vec{r}) \underbrace{\frac{N_t}{2} Im\{\exp(-i(\vec{k}_{mn}(\vec{r})\cdot\vec{r} + \phi_{mn}(\vec{r})))\}}_{\substack{\text{Harmonic}\\ \text{Frequency}\\ \text{Selection}}} \tag{AP. 7}$$

$$SD[Re\{\hat{u}_{mn}(\vec{r})\}] = SD[Im\{\hat{u}_{mn}(\vec{r})\}] = \frac{1}{{}^{i}\Psi_{mn}(\vec{r})} \underbrace{\sqrt{\frac{N_t}{2}}}_{\substack{\text{Harmonic}\\ \text{Frequency}\\ \text{Selection}}} \underbrace{\sqrt{\sum_{x=-2}^{2}\sum_{y=-2}^{2}(h_{GK}(\vec{r}))^2}}_{\text{Smoothing}} \tag{AP. 8}$$

where N_t is the number of discrete Fourier transform (DFT) points used in harmonic frequency selection, equivalently, the number of phase offsets. Note that for a high SNR, the effect of unwrapping on the SNR is absent. The unwrapping algorithm is Laplacian based.[23]

Then, directional filtering by $Z_l(\vec{k})$ takes place, which is given as:

$$Z_l(\vec{k}) = \beta(\vec{k})\exp\left(-\frac{\left(\arg\{\vec{k}\} - \phi_{Z_l}\right)^2}{2\sigma_Z^2}\right), \tag{AP.9}$$

where the radial filtering component is:

$$\beta(\vec{k}) = \frac{1}{1 + \left(\frac{k}{k_{up}}\right)^{2N}} - \frac{1}{1 + \left(\frac{k}{k_{low}}\right)^{2N}}. \tag{AP.10}$$

and $\sigma_Z = 2\pi/N_l$. In equation Equation (AP. 5), arg returns angle of the vector. Note that ϕ_{Z_l} is the direction of the lth directional filter, N_l is the number of directional filters, N is the filter order, and k_{low} and k_{up} are lower and upper cut-off values in the k-space, respectively. In the simulations and experiments, the directional filter parameters are selected as: N=10, $k_{low} = 0.02\Delta^{-1}$ and $k_{up} = 0.5\Delta^{-1}$, where Δ is the in-plane voxel size, which is assumed to be isotropic here. After the directional filtering, the statistics of the noise become:

$$E[Re\{\hat{u}_{lmn}(\vec{r})\}] = u_{0lmn}(\vec{r}) \underbrace{\frac{N_t}{2} Re\{\exp(-i(\vec{k}_{lmn}(\vec{r})\cdot\vec{r} + \phi_{lmn}(\vec{r})))\}}_{\text{Harmonic Frequency Selection}} \underbrace{Z_l(\vec{k}_{lmn})}_{\text{Directional Filter}} \tag{AP. 11}$$

$$E[Im\{\hat{u}_{lmn}(\vec{r})\}] = u_{0lmn}(\vec{r}) \underbrace{\frac{N_t}{2} Im\{\exp(-i(\vec{k}_{lmn}(\vec{r})\cdot\vec{r} + \phi_{lmn}(\vec{r})))\}}_{\text{Harmonic Frequency Selection}} \underbrace{Z_l(\vec{k}_{lmn})}_{\text{Directional Filter}}, \tag{AP. 12}$$

$$SD[Re\{\hat{u}_{lmn}(\vec{r})\}] = SD[Im\{\hat{u}_{lmn}(\vec{r})\}] = \frac{1}{{}^{i}\Psi_{mn}(\vec{r})} \underbrace{\sqrt{\frac{N_t}{2}}}_{\text{Harmonic Frequency Selection}} \underbrace{\alpha}_{\text{Smoothing and Directional Filter}} \tag{AP. 13}$$

where $Z_l(\vec{k}_{lmn})$ is the response of the l^{th} directional filter at $\vec{k}_{lmn}$ and α is given as:

$$\alpha = \sqrt{\sum_{x=-N_x/2}^{N_x/2-1} \sum_{y=-N_y/2}^{N_y/2-1} \left(h_{GK}\left(\vec{r}\right) ** \zeta_l\left(\vec{r}\right)\right)^2}, \tag{AP.14}$$

where $\zeta_l\left(\vec{r}\right) = F_{2D}^{-1}\{Z_l(\vec{k})\}$, and $**$ is the 2D convolution operator.

Here, we assume $Z_l(\vec{k}_{lmn}) = 1$ if the $\mathrm{l}^t h$ direction is the propagation direction of the plane wave, which may not always be true but is very close to 1 for most of the cases; otherwise, it is zero. Thus, we drop the term $Z_l(\vec{k}_{lmn})$ for the rest of the derivation. Therefore, the magnitude of SNR of directionally filtered displacement in the direction of the plane wave propagation, ${}^{u}\Psi$, can be expressed as:

$${}^{u}\Psi_{lmn}\left(\vec{r}\right) = {}^{i}\Psi_{mn}\left(\vec{r}\right) \frac{u_{0lmn}\left(\vec{r}\right)\sqrt{N_t}}{\sqrt{2}\alpha} \tag{AP.15}$$

Then, directionally filtered displacement is normalized by its magnitude $\hat{u}_{lmn}\left(\vec{r}\right)/|\hat{u}_{lmn}\left(\vec{r}\right)|$. The expected and SD value of $\exp\left(i\hat{\vec{k}}_{lmn}\cdot\vec{r}\right)$ is:

$$E[Re\{\hat{u}_{lmn}\left(\vec{r}\right)/|\hat{u}_{lmn}\left(\vec{r}\right)|\}] = Re\left\{\exp\left(-i\left(\vec{k}_{lmn}\left(\vec{r}\right)\cdot\vec{r} + \phi_{lmn}\left(\vec{r}\right)\right)\right)\right\} \tag{AP.16}$$

$$E[Im\{\hat{u}_{lmn}\left(\vec{r}\right)/|\hat{u}_{lmn}\left(\vec{r}\right)|\}] = Im\left\{\exp\left(-i\left(\vec{k}_{lmn}\left(\vec{r}\right)\cdot\vec{r} + \phi_{lmn}\left(\vec{r}\right)\right)\right)\right\} \tag{AP.17}$$

$$SD[Re\{\hat{u}_{lmn}(\vec{r})/|\hat{u}_{lmn}(\vec{r})|\}] = \frac{1}{{}^{i}\Psi_{mn}(\vec{r})} \underbrace{\sqrt{\frac{N_t}{2}}}_{\text{Harmonic Frequency Selection}} \underbrace{\alpha}_{\text{Smoothing and Directional Filter}} \underbrace{\frac{2|Re\{i\exp(-i(\vec{k}_{lmn}(\vec{r})\cdot\vec{r} + \phi_{lmn}(\vec{r})))\}|}{N_t u_{0lmn}}}_{\text{Normalization}} \tag{AP. 18}$$

$$SD[Im\{\hat{u}_{lmn}(\vec{r})/|\hat{u}_{lmn}(\vec{r})|\}] = \frac{1}{{}^{i}\Psi_{mn}(\vec{r})} \underbrace{\sqrt{\frac{N_t}{2}}}_{\text{Harmonic Frequency Selection}} \underbrace{\alpha}_{\text{Smoothing and Directional Filter}} \underbrace{\frac{2|Im\{i\exp(-i(\vec{k}_{lmn}(\vec{r})\cdot\vec{r} + \phi_{lmn}(\vec{r})))\}|}{N_t u_{0lmn}}}_{\text{Normalization}} \tag{AP. 19}$$

Computing L2-norm of in-plane gradients:

$$\hat{k}_{lmn}\left(\vec{r}\right) = \sqrt{\left|\frac{\partial}{\partial x}\frac{\hat{u}_{lmn}\left(\vec{r}\right)}{|\hat{u}_{lmn}\left(\vec{r}\right)|}\right|^2 + \left|\frac{\partial}{\partial y}\frac{\hat{u}_{lmn}\left(\vec{r}\right)}{|\hat{u}_{lmn}\left(\vec{r}\right)|}\right|^2}, \tag{AP.20}$$

and

$$E[\hat{k}_{lmn}\left(\vec{r}\right)] = \|\vec{k}_{lmn}\left(\vec{r}\right)\| = k_{lmn}\left(\vec{r}\right) \tag{AP.21}$$

$$SD[\hat{k}_{lmn}(\vec{r})] = \frac{1}{{}^{i}\Psi_{mn}(\vec{r})} \underbrace{\sqrt{\frac{N_t}{2}}}_{\substack{\text{Harmonic}\\ \text{Frequency}\\ \text{Selection}}} \underbrace{\alpha}_{\substack{\text{Smoothing}\\ \text{and}\\ \text{Directional}\\ \text{Filter}}} \underbrace{\frac{2}{N_t u_{0\,lmn}(\vec{r})}}_{\text{Normalization}} \underbrace{\frac{1}{\sqrt{2}\Delta}}_{\substack{\text{In-plane}\\ \text{Gradients}}} . \tag{AP. 22}$$

In the equation above, $\hat{k}_{lmn}$ is the estimate of k_{lmn}.

Hence, the SNR of the wavenumber reconstructed is $SNR_{\hat{k}} = E[\hat{k}_{lmn}]/SD[\hat{k}_{lmn}]$. Then, the inverse of the wave speed is computed $\hat{c}_{lmn}^{-1} = \hat{k}_{lmn}/\omega_n$. Note that $SNR_{\hat{c}^{-1}} = SNR_{\hat{k}}$ because the mean and SD are both scaled by $1/\omega_n$ (i.e., $E[\hat{c}^{-1}] = E[\hat{k}_{lmn}]/\omega_n$ and $SD[\hat{c}^{-1}] = SD[\hat{k}_{lmn}]/\omega_n$), resulting in no change in the SNR. Additionally, using linearization via Taylor series, it can be shown that $SNR_{\hat{c}} = SNR_{\hat{c}^{-1}}$, where $SNR_{\hat{c}}$ is the SNR of $\hat{c}$.